PCCP

COMMUNICATION

View Article Online
View Journal | View Issue

Cite this: *Phys. Chem. Chem. Phys.*, 2024, **26**, 11277

Received 20th September 2023,
Accepted 2nd January 2024

DOI: 10.1039/d3cp04581a

rsc.li/pccp

A chiral metal cluster triggers enantiospecific electronic transport†

Omar Hernández-Montes, [a] Ignacio L. Garzón [b] and J. Eduardo Barrios-Vargas *[a]

Chirality is a geometric property of matter that can be present at different scales, especially at the nanoscale. Here, we investigate the manifestation of chirality in electronic transport through a molecular junction. Spinless electronic transport through a chiral molecular junction is not enantiospecific. However, when a chiral metal cluster, C_3-Au_{34}, is attached to the source electrode, a different response is obtained in spinless electronic transport between R and L systems: this indicates the crucial role of chiral clusters in triggering enantiospecific spinless electronic transport. In contrast, when an achiral metal cluster, C_{3v}-Au_{34}, is attached, no change in conductance occurs between enantiomeric systems. Using the non-equilibrium green's function method, we characterized this phenomenon by calculating the transmission and conductance of spin-unpolarized electrons. Our theoretical results highlight the importance of metal clusters with specific sizes and chiral structures in electronic transport and support previously published experimental results that exhibited enantiospecific scanning tunneling measurements with intrinsically chiral tips.

Chirality is a geometric property of matter present at every scale in the universe. At the nanoscale, it has been studied in bare and ligand-protected metal clusters and nanoparticles.[1,2] In these studies, chirality has been detected through its physical and chemical manifestations. In the first case, chiral nanostructures may interact with circularly polarized light to display a nonzero circular dichroism spectrum.[2] Chirality is also chemically expressed when two chiral systems interact with each other, inducing the phenomenon of chiral molecular recognition.[2,3] In this work, a third mechanism of manifestation of chirality is proposed by utilizing a chiral bare metal cluster to modify a molecular junction that triggers enantiospecific electronic transport.

Electronic transport at the nanoscale has been broadly investigated, partly motivated by the miniaturization of electronic devices and the need to disclose novel phenomena in such devices.[4–6] On the one hand, the conductance in metallic short wires is quantized and depends on the length and cross section.[7–9] On the other hand, novel phenomena have been discovered when a molecule is used instead of a metallic nanostructure. For example, when a current passes through chiral molecules, transport depends on the spin of the electron, which is determined by the handedness of the molecule and the direction of motion.[10] This effect, called chiral-induced spin selectivity (CISS), shows the importance of molecular chirality in molecular electronics and spintronics.[11]

One question to investigate is whether enantiospecific electronic transport could be achieved as a result of the presence of chiral clusters at molecular junctions. This work theoretically investigates this possibility by calculating the transmission coefficient of spin-unpolarized electrons moving through a chiral-modified molecular junction. Indeed, our results show that enantiospecific transport is obtained for electrons independently of their spin when the first electrode (source) is modified by attaching a chiral metal cluster to its surface before the electron current passes through chiral molecules towards the second (drain) electrode. In this way, the wave function amplitude and phase of the departing electrons from one side of the junction are modified when they interact with the chiral electron density of the attached cluster.

This type of enantiospecific electron transport has not been widely discussed before. However, a related proposal has been made by Liu *et al.* in ref. 12. They achieved real-time chiral recognition using the enantiospecific interaction of the β-cyclodextrin molecular machine with different amino acids, manifesting as a different electrical response when the system is connected to graphene electrodes. Also, Tierney *et al.* in ref. 13 suggested the existence of intrinsic chirality in regular scanning tunneling microscope (STM) tips, which leads to

[a] *Departamento de Física y Química Teórica, Facultad de Química, Universidad Nacional Autónoma de México, Ciudad de México 04510, Mexico. E-mail: omar.hdz.mon@gmail.com, j.e.barrios@gmail.com*

[b] *Instituto de Física, Universidad Nacional Autónoma de México, Apartado Postal 20-364, Ciudad de México 01000, Mexico. E-mail: garzon@fisica.unam.mx*

† Electronic supplementary information (ESI) available. See DOI: https://doi.org/10.1039/d3cp04581a

different electron tunneling efficiencies through left- and right-handed molecules, with no need for a magnetized STM tip, as required in the CISS effect. More recently, a theoretical study reported a systematic study on the emergence of spin-polarization caused by electrodes in molecular junctions with reduced (chiral) symmetries.[14]

Chiral molecule

The present study focuses on electronic transport through a chiral viologen molecule (see Fig. 1a and b). Viologen molecules form a set of organic molecules that have been used as linkers of nitrogenous bases and amino acids,[15] to anchor Ag nanoparticles to graphene oxide,[16] also widely used as building blocks of molecular machines,[17] and more recently in STM breaking junctions for molecular electronics studies.[18–20] Specifically, we consider the chiral HB viologen molecule, which has recently been synthesized.[21] Its structure can be decomposed into an achiral backbone (VB, viologen backbone) displayed in Fig. 1a. The chiral HB viologen is formed by the VB plus two phenyl rings attached to the VB's middle part by a quinoxaline bridge. These phenyl rings have different orientations to each other, providing chirality to the HB viologen molecule, as depicted in Fig. 1b. This chirality can be measured by calculating the Hausdorff Chirality Measure (HCM).[22] The HCM quantifies the degree of overlap between enantiomers using the Hausdorff distance between their sets of atoms. Comparisons between chiral cluster structures with different HCM values have been made for bare and ligand-protected gold clusters.[23] In this way, HCM allows us to verify that VB is achiral (HCM = 0.0) and to assess the degree of chirality of the chiral HB viologen (HCM = 0.14).

Modified molecular junctions

These devices are composed of two crystalline gold electrodes at the ends of the molecular junction, then an achiral (or a chiral) Au_{34} gold cluster is attached to the left (source) electrode, and finally, at the middle part of these molecular devices, viologen-like molecules (VB and both HB enantiomers) are connected on their left side to the achiral (or chiral) cluster and their right side to the drain electrode, and also, the electrodes were modeled with a FCC lattice exposing the surface (100). For the achiral gold cluster C_{3v}-Au_{34} (here labeled $achAu_{34}$, see Fig. 1c), a HCM = 0.0 value is obtained. Unlike that, the chiral metal gold cluster C_3-Au_{34} (here named $chAu_{34}$, see Fig. 1d), has a non-zero index of chirality: HCM = 0.12.[2,24–27] In this work, we focus on three different molecular junctions to study electronic transport systematically: (1) an unmodified pristine molecular junction (no clusters are attached), (2) an achiral-modified molecular junction (with the presence of $achAu_{34}$), and finally (3) a chiral-modified molecular junction (with the presence of $chAu_{34}$).‡

Electronic transport through the modified molecular junctions described above was characterized by calculating the transmission function, *I–V* curves, and conductance using the TranSIESTA[28] module integrated into the *ab initio* materials program based on the density functional theory called SIESTA.[29,30] TranSIESTA enables the modeling of nonequilibrium electronic transport using the Green's function formalism[31–33] (further details about the calculation of electronic transport quantities are shown in S1 ESI†).

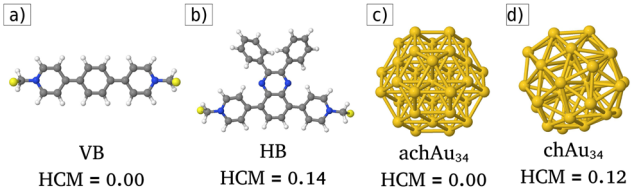

Fig. 1 (a) Viologen backbone (VB), (b) chiral HB viologen, (c) achiral metal cluster $achAu_{34}$ and (d) chiral metal cluster $chAu_{34}$. The calculated Hausdorff chirality measure (HCM) is displayed beneath each picture.

In the first case (see Fig. 2a–c), we calculate the transmission function of single molecular junctions considering the current traveling from the pristine source electrode through the VB and the *R* and *L* enantiomers of the chiral HB molecule (HBR and HBL). Fig. 2d displays the corresponding transmission functions: the yellow curve corresponds to the VB case, the red curve for HBR, and the blue curve for HBL. These functions are similar in every case (see Fig. 2d); consequently, this similarity manifests itself as similar slopes (or conductance *G*) in the ohmic region (linear dependence region in the range 0–0.25 V) in the *I–V* curves (see Fig. 2e). After linear fitting the *I–V* curves for the two enantiomers HBR and HBL, their corresponding conductance is $G = 36.7\ \mu A\ V^{-1}$ and $G = 36.5\ \mu A\ V^{-1}$, respectively. These values indicate that, for the pristine molecular junction case, in the ohmic region, both enantiomers have a very similar electronic transport behavior without any enantiospecific effect. In other words, enantiospecific electronic transport is not present for single-molecular junctions. This result is consistent with previous calculations of molecule carbon rings; further details of the calculation parameters are available in S2 ESI.†

In the second case, an achiral $achAu_{34}$ gold cluster is placed on the surface of the source electrode, considering an Au–Au distance equal to 2.5 Å, without performing any geometric optimization. Furthermore, the VB, HBR, and HBL molecules are also connected to the $achAu_{34}$ cluster with an Au–S distance (2.60 Å) in the bridge configuration, which has been previously obtained in other calculations of Au clusters protected by thiol.[3,27,34] These achiral-modified molecular junctions are displayed in Fig. 3a–c. Also, Fig. 3d displays their respective transmission functions, indicating a behavior similar to that obtained for the pristine source electrode. Therefore, in this achiral-modified electrode configuration, no enantiospecific electronic transport was achieved; however, lower conductance values were obtained compared to the pristine case (see the corresponding slopes in the *I–V* curves in Fig. 3e).

In the third case, chiral-modified molecular junctions were built by attaching the chiral metal cluster $chAu_{34}$ to the surface

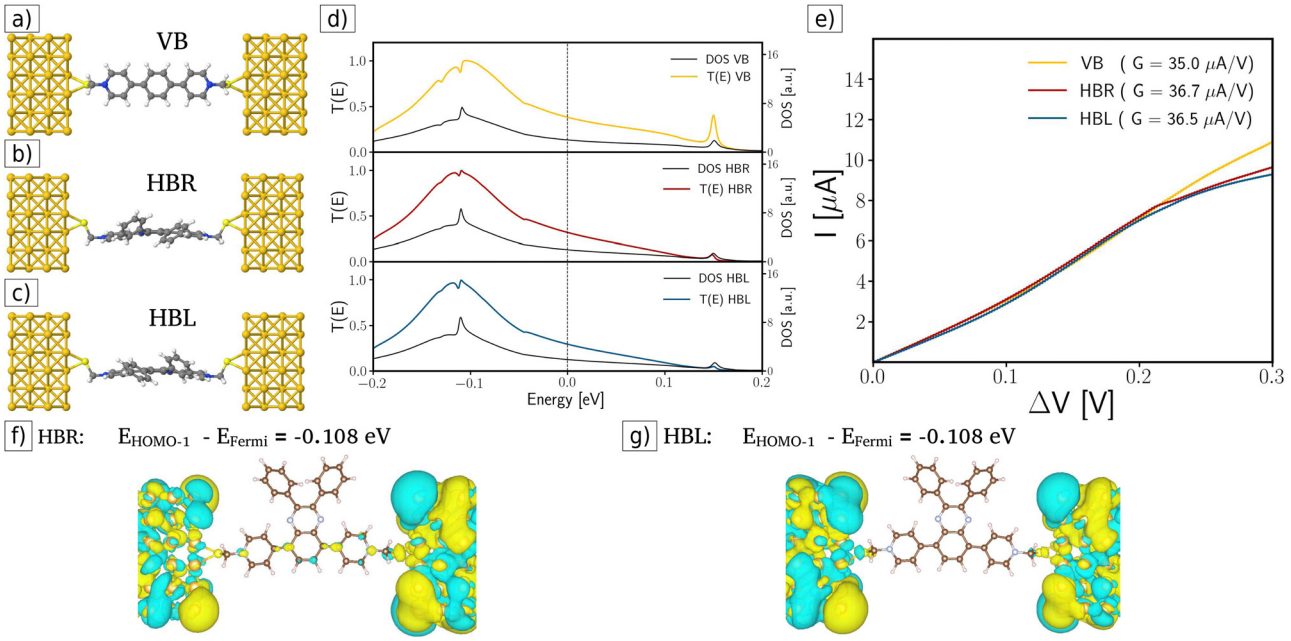

Fig. 2 Chiral molecular junctions connected to pristine gold electrodes for (a) VB (front view), (b) HBR (top view), and (c) HBL (top view); the electrodes were modeled with an FCC lattice exposing the (100) surface. It is worth mentioning that the chirality of the system emerges from the spatial orientation of the phenyl rings. (d) Transmission functions for VB (yellow), HBR (red), and HBL (blue); additionally, the density of states (DOS) is plotted as a black curve (the vertical black dashed line indicates Fermi's energy position at 0.0 eV). (e) Current–bias voltage plots (I–V curve) for VB (yellow), HBR (red), and HBL (blue). Furthermore, the molecular orbital HOMO−1 of the scattering region for (f) HBR and (g) HBL is shown; as can be observed, they do not exhibit significant differences between them. The yellow color indicates positive values, while the cyan color exhibits negative values. These molecular orbitals were obtained using a functional GGA/PBE, a base size DZP, and an isosurface value of 0.006 $Å^{-3/2}$.

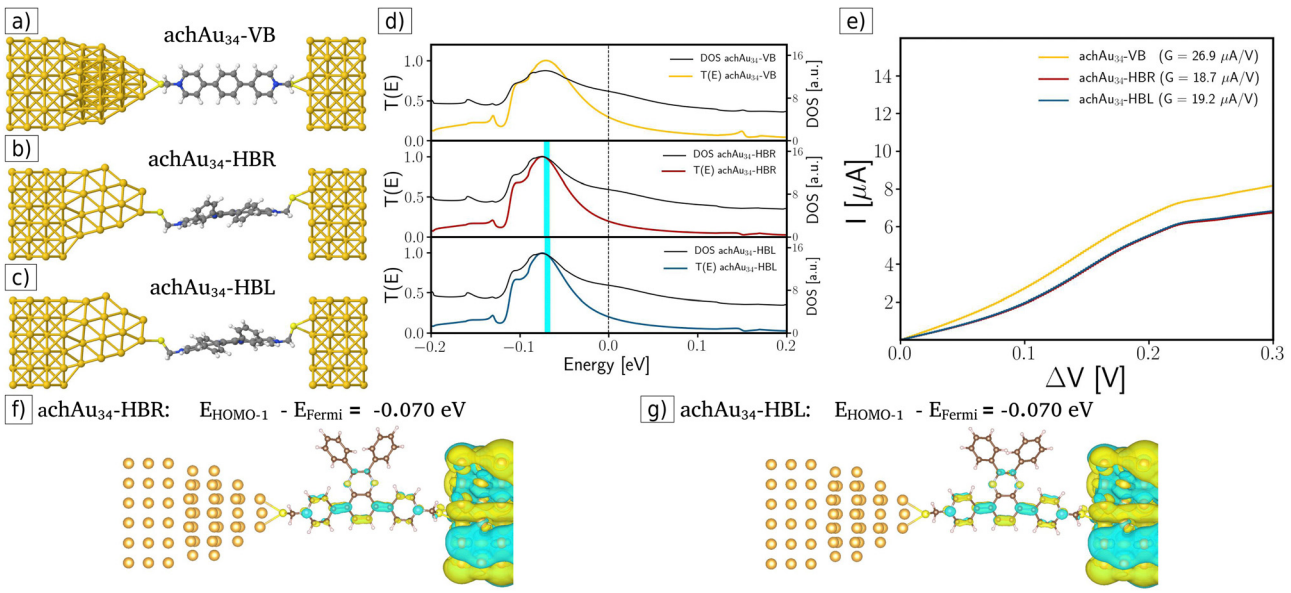

Fig. 3 Achiral-modified molecular junctions for (a) achAu$_{34}$-VB (front view), (b) achAu$_{34}$-HBR (top-view), and (c) achAu$_{34}$-HBL (top-view). (d) Transmission functions for achAu$_{34}$-VB (yellow), achAu$_{34}$-HBR (red), and achAu$_{34}$-HBL (blue); in each case, the DOS is plotted as a black curve. Additionally, the energy positions of HOMO−1 for the scattering region of achAu$_{34}$-HBR,L are indicated with a cyan bar close to the maximum DOS. (e) Current–bias voltage curves for achAu$_{34}$-VB (yellow), achAu$_{34}$-HBR (red), and achAu$_{34}$-HBL (blue). This figure shows that enantioselective transport does not occur when the achAu$_{34}$ cluster is attached. Furthermore, the molecular orbital HOMO−1 of the scattering region for (f) achAu$_{34}$-HBL and (g) achAu$_{34}$-HBR is shown; as can be observed, they do not exhibit significant differences between them. The yellow color indicates positive values, while the cyan color exhibits negative values. These molecular orbitals were obtained using a functional GGA/PBE, a base size DZP, and an isosurface value of 0.006 $Å^{-3/2}$.

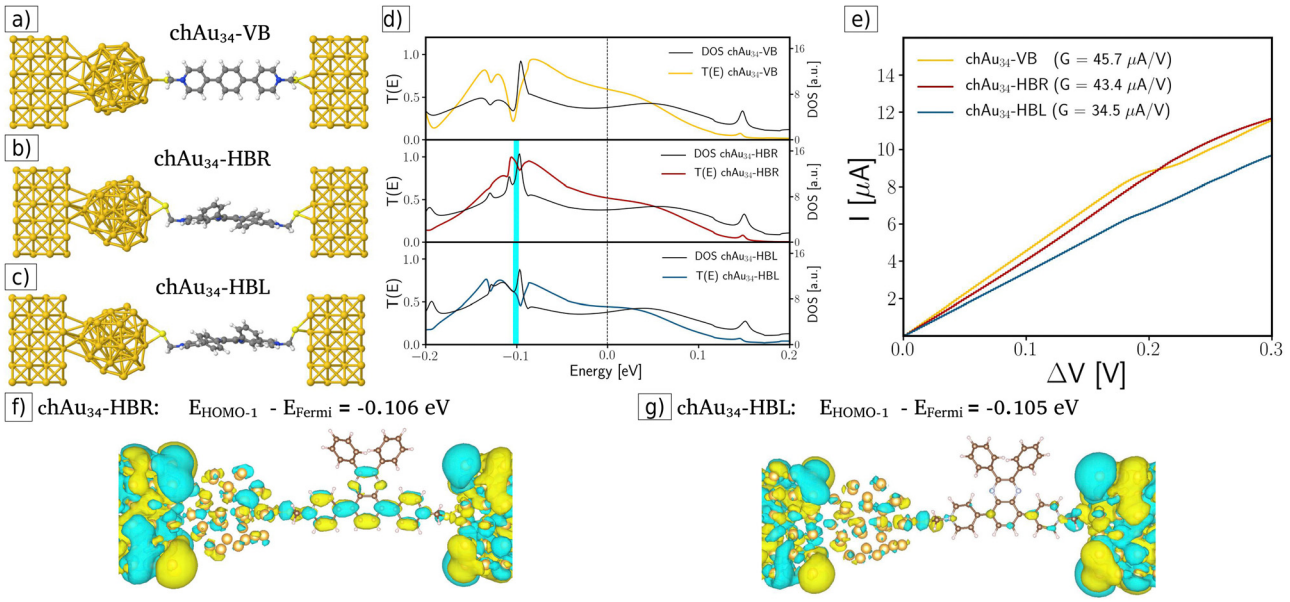

Fig. 4 Chiral-modified molecular junctions when the $chAu_{34}$ chiral cluster is attached to the source electrode: (a) $chAu_{34}$-VB (front view), (b) $chAu_{34}$-HBR (top-view), and (c) $chAu_{34}$-HBL (top-view). (d) Transmission functions for $chAu_{34}$-VB (yellow), $chAu_{34}$-HBR (red), and $chAu_{34}$-HBL (blue) in each case; the DOS is plotted as a black curve. Additionally, the energy positions of HOMO−1 for the scattering region of $chAu_{34}$-HBR,L are indicated with a cyan bar close to the maximum DOS. (e) Current–bias voltage curves for: $chAu_{34}$-VB (yellow), $chAu_{34}$-HBR (red), and $chAu_{34}$-HBL (blue). In this case, enantiospecific electronic transport is visualized in the ohmic region. Furthermore, the molecular orbitals of HOMO−1 of the scattering region for (f) $chAu_3$4-HBL and (g) $chAu_{34}$-HBR are shown; this time, for the $chAu_{34}$-HBL case a higher localization of the HOMO−1 orbital is obtained in comparison with the $chAu_{34}$-HBR one. This difference in amplitude generates a pronounced difference in conductance. The yellow color indicates positive values, while the cyan color exhibits negative values. These molecular orbitals were obtained using a functional GGA/PBE, a basis size DZP, and an isosurface value of 0.006 $Å^{-3/2}$.

of the left-handed electrode (see Fig. 4a–c). By analyzing the transmission coefficients, DOS, and *I*–*V* curves displayed in Fig. 4d and e, clear evidence for enantiospecific electronic transport was obtained. For example, in the ohmic region (see Fig. 4e) the transport is favored for the $chAu_{34}$-HBR system, which increases the conductance by 20% with respect to the $chAu_{34}$-HBL case: $G_{chAu_{34}\text{-HBR}}$ (43.4 μA V^{-1}) > $G_{chAu_{34}\text{-HBL}}$ (34.5 μA V^{-1}). The origin of this enantiospecific electronic transport is related to a significant difference in transmission functions and DOS at energies around −0.1 eV. For example, the transmission drop-off in the $chAu_{34}$-HBL case and the maximum transmission for the $chAu_{34}$-HBR enantiomer occurs at energies around −0.1 eV, between the energy values of the HOMO and HOMO−1 eigenstates. Fig. 4d shows a plot of the transmission function for the chiral-modified case, in which it is indicated with a cyan bar the position of the HOMO−1 eigenstate. Fig. 4f and g show the amplitude of the HOMO−1 molecular orbitals for each case. These figures show that the HOMO−1 of the $chAu_{34}$-HBL enantiomer is more localized than the HOMO−1 for the $chAu_{34}$-HBR one. Then, the drop in the transmission function for the $chAu_{34}$-HBL case, around −0.1 eV, is due to a higher localization of its molecular orbital HOMO−1 mainly along the backbone region (see Fig. 4f). Moreover, Fig. 4g shows that the amplitude of the HOMO−1 orbital is highly delocalized for the $chAu_{34}$-HBR enantiomer, which is consistent with a maximum of the transmission function, in contrast with the $chAu_{34}$-HBL case in which transmission decreases. It should be noted that these results are a consequence of the $chAu_{34}$ presence in the chiral-modified case since the delocalized orbital was not obtained in the achiral-modified case (see Fig. 3f and g). Therefore, the molecule's handedness induced a higher delocalization in the HBR enantiomer than in the HBL one.

Another quantitative way to prove the enantiospecific effect in electronic transport is through the difference in the transmission as an energy function between the *R*- and *L*-enantiomeric systems. Fig. 5 shows this difference for the pristine case (orange curve), the achiral-modified case (blue curve), and the chiral-modified one (red curve). From the graph previously mentioned, it is possible to compare the three setups here analyzed and see that, definitively, the $chAu_{34}$ metal cluster brings out a significant difference in the probability of transmission of electrons in chiral systems. Additionally, the degree of localization/delocalization of the HOMO−1 orbitals provides a simple explanation for the origin of enantiospecific electronic transport in the chiral-modified molecular junction.

To provide additional insights into the mechanisms responsible for the enantiospecific electron transport described above, the orbital occupancy of the carbon and sulfur atoms in the achiral- and chiral-modified molecular junctions was investigated by calculating the difference in the projected density of states (PDOS) between the HBR and HBL cases (see S3 ESI† section for a description and figures of the PDOS). From these calculations, it was found that, for the achiral case, the p-like orbitals of the carbon and sulfur atoms do not show a significant difference between the HBL and HBR cases

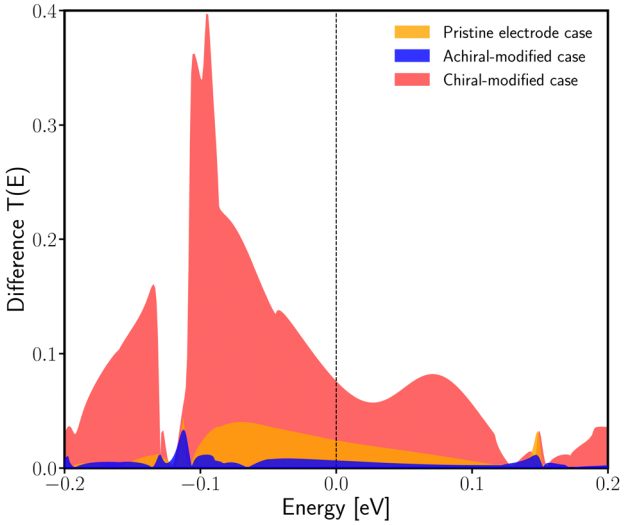

Fig. 5 Difference of the transmission functions between the HBR and HBL cases as a function of energy, for the pristine (orange curve), achiral-modified (blue curve), and chiral-modified (red curve) molecular junctions. For the chiral-modified one, several broad peaks exist that induce the difference in the *I*–*V* curves, in contrast with the pristine case, where shorter and narrower peaks were obtained.

(see Fig. S3c and d, respectively, ESI†). On the contrary, in the case of the chiral-modified molecular junctions, there is a significant difference in PDOS between the HBR and HBL cases, particularly for the C $2p_y$ and S $3p_y$ orbitals (see Fig. S4c and d, respectively, ESI†). Therefore, these results indicate that the p-like orbitals of the carbon and sulfur atoms have a similar orbital occupancy when an achiral cluster is present, but the opposite behavior (different orbital occupancy) is obtained when a chiral cluster modifies the gold electrode. These results provide further insights into the relationship of the enantiospecific electron transport with the different orbital angular momentum of the transmitted electrons. This orbital-related mechanism is consistent with recent results claiming that the orbital occupancy (polarization), caused by a lowering of the symmetry or a distortion of the atomic structure, determines chemical and physical properties such as electron transport (see, for example: Lee *et al.* 2021 in ref. 35 and Do and Lee 2022 in ref. 36).

One remaining question concerns the relationship between the present results and those obtained using chiral STM tips.[13] The chiral-modified molecular junction investigated in this study could be proposed as a theoretical model for the experimental setup discussed in ref. 13. On the basis of the above results, the chiral-modified molecular junction better describes the experimental situation. This indicates that the STM tip requires a chiral shape at the very end of the tip to obtain enantiospecific electron transmission efficiencies.

Final remarks

By attaching a chiral metal cluster Au_{34} to the surface of a pristine source electrode and, at the same time, connecting to a chiral HB molecule, enantiospecific electronic transport was achieved. As exposed, the localization/delocalization of the principal transmission channel (HOMO−1) was the key feature that underlies the enantiospecific transport. For this achievement, it was necessary to maintain the chiral structure of the C_3-Au_{34} cluster attached to the source electrode.

It is worth mentioning that the enantiospecific electron transport predicted in this study is independent of spin, in contrast to the CISS effect. However, in both cases, molecular chirality plays an important role, either by modifying the electron wave function passing through a chiral metal cluster or coupling the spin to the electron density of a chiral molecule.

The present study is expected to motivate further theoretical studies looking for additional features related to enantiospecific electronic transport and cluster electronics applications.[37] At the same time, further experimental work that clarifies the role of chiral STM tips in enantioselective electron tunneling efficiencies would be desirable.

Author contributions

All the authors contributed to the planning of the investigation. OHM carried out the numerical calculations and wrote a draft of the main results and the manuscript, which all the authors improved.

Conflicts of interest

There are no conflicts to declare.

Acknowledgements

OHM acknowledges CONAHCYT for a graduate student scholarship. JEBV acknowledges funding from CONAHCYT Frontera 428214 and PAIP-FQ(UNAM) 5000-9173. ILG thanks the funding of CONAHCYT-Mexico under Project 285821, DGAPA-UNAM-Mexico under Project IN106021, and DGTIC-UNAM-Mexico under Project LANCAD 049.

Notes and references

‡ The atomic coordinates of bonded viologens to $chAu_{34}$ are available in: for HBR **https://github.com/jebarriosvargas/PCCP_D3CP04581A/blob/2ac6373d2bffaf2a9e8e92ef24416b3a99a05376/au34_hb3R.pdb** and HBL **https://github.com/jebarriosvargas/PCCP_D3CP04581A/blob/2ac6373d2bffaf2a9e8e92ef24416b3a99a05376/au34_hb3L.pdb**.

1 J. M. Hicks, The Physical Chemistry of Chirality, *Chirality: Physical Chemistry*, American Chemical Society, 2002, pp. 2–16.
2 J. J. Pelayo, I. Valencia, A. P. Garcáa, L. Chang, M. López, D. Toffoli, M. Stener, A. Fortunelli and I. L. Garzón, *Adv. Phys.: X*, 2018, **3**, 1509727.
3 X. López-Lozano, L. A. Pérez and I. L. Garzón, *Phys. Rev. Lett.*, 2006, **97**, 233401.
4 A. Nitzan and M. A. Ratner, *Science*, 2003, **300**, 1384–1389.
5 M. L. Perrin, E. Burzurí and H. S. J. van der Zant, *Chem. Soc. Rev.*, 2015, **44**, 902–919.

6 F. Evers, R. Korytár, S. Tewari and J. M. van Ruitenbeek, *Rev. Mod. Phys.*, 2020, **92**, 035001.
7 J. I. Pascual, J. Méndez, J. Gómez-Herrero, A. M. Baró, N. Garcia, U. Landman, W. D. Luedtke, E. N. Bogachek and H. P. Cheng, *Science*, 1995, **267**, 1793–1795.
8 M. Brandbyge, J. Schiøtz, M. R. Sørensen, P. Stoltze, K. W. Jacobsen, J. K. Nørskov, L. Olesen, E. Laegsgaard, I. Stensgaard and F. Besenbacher, *Phys. Rev. B: Condens. Matter Mater. Phys.*, 1995, **52**, 8499–8514.
9 N. Agraït, A. L. Yeyati and J. M. van Ruitenbeek, *Phys. Rep.*, 2003, **377**, 81–279.
10 R. Naaman and D. H. Waldeck, *J. Phys. Chem. Lett.*, 2012, **3**, 2178–2187.
11 R. Naaman and D. H. Waldeck, *Annu. Rev. Phys. Chem.*, 2015, **66**, 263–281.
12 Z. Liu, X. Li, H. Masai, X. Huang, S. Tsuda, J. Terao, J. Yang and X. Guo, *Sci. Adv.*, 2021, **7**, eabe4365.
13 H. L. Tierney, C. J. Murphy and E. C. H. Sykes, *Phys. Rev. Lett.*, 2011, **106**, 010801.
14 W. Dednam, M. A. García-Blázquez, L. A. Zotti, E. B. Lombardi, C. Sabater, S. Pakdel and J. J. Palacios, *ACS Nano*, 2023, **17**, 6452–6465.
15 L. Barravecchia, I. Neira, E. Pazos, C. Peinador and M. D. García, *J. Org. Chem.*, 2022, **87**, 760–764.
16 S. Krishnamurthy, I. V. Lightcap and P. V. Kamat, *J. Photochem. Photobiol., A*, 2011, **221**, 214–219.
17 H. Chen and J. Fraser Stoddart, *Nat. Rev. Mater.*, 2021, **6**, 804–828.
18 A. Borges, E.-D. Fung, F. Ng, L. Venkataraman and G. C. Solomon, *J. Phys. Chem. Lett.*, 2016, **7**, 4825–4829.
19 Q. V. Nguyen, P. Martin, D. Frath, M. L. Della Rocca, F. Lafolet, S. Bellinck, P. Lafarge and J.-C. Lacroix, *J. Am. Chem. Soc.*, 2018, **140**, 10131–10134.
20 H. Chen, H. Zheng, C. Hu, K. Cai, Y. Jiao, L. Zhang, F. Jiang, I. Roy, Y. Qiu, D. Shen, Y. Feng, F. M. Alsubaie, H. Guo, W. Hong and J. F. Stoddart, *Matter*, 2020, **2**, 378–389.
21 Z. Ding, H. Chen, Y. Han and J. Liu, *J. Mol. Struct.*, 2022, **1262**, 133073.
22 I. L. Garzón, J. A. Reyes-Nava, J. I. Rodríguez-Hernández, I. Sigal, M. R. Beltrán and K. Michaelian, *Phys. Rev. B: Condens. Matter Mater. Phys.*, 2002, **66**, 073403.
23 J. J. Pelayo, R. L. Whetten and I. L. Garzón, *J. Phys. Chem. C*, 2015, **119**, 28666–28678.
24 I. E. Santizo, F. Hidalgo, L. A. Pérez, C. Noguez and I. L. Garzón, *J. Phys. Chem. C*, 2008, **112**, 17533–17539.
25 A. Lechtken, D. Schooss, J. R. Stairs, M. N. Blom, F. Furche, N. Morgner, O. Kostko, B. von Issendorff and M. M. Kappes, *Angew. Chem., Int. Ed.*, 2007, **46**, 2944–2948.
26 X. Gu, S. Bulusu, X. Li, X. C. Zeng, J. Li, X. G. Gong and L.-S. Wang, *J. Phys. Chem. C*, 2007, **111**, 8228–8232.
27 J. J. Pelayo, I. Valencia, G. Díaz, X. Lopez-Lozano and I. L. Garzón, *Eur. Phys. J. D*, 2015, **69**, 1–7.
28 M. Brandbyge, J.-L. Mozos, P. Ordejón, J. Taylor and K. Stokbro, *Phys. Rev. B: Condens. Matter Mater. Phys.*, 2002, **65**, 165401.
29 J. M. Soler, E. Artacho, J. D. Gale, A. García, J. Junquera, P. Ordejón and D. Sánchez-Portal, *J. Condens. Matter Phys.*, 2002, **14**, 2745.
30 A. García, N. Papior, A. Akhtar, E. Artacho, V. Blum, E. Bosoni, P. Brandimarte, M. Brandbyge, J. I. Cerdá, F. Corsetti, R. Cuadrado, V. Dikan, J. Ferrer, J. Gale, P. García-Fernández, V. M. García-Suárez, S. García, G. Huhs, S. Illera, R. Korytár, P. Koval, I. Lebedeva, L. Lin, P. López-Tarifa, S. G. Mayo, S. Mohr, P. Ordejón, A. Postnikov, Y. Pouillon, M. Pruneda, R. Robles, D. Sánchez-Portal, J. M. Soler, R. Ullah, V. W.-Z. Yu and J. Junquera, *J. Chem. Phys.*, 2020, **152**, 204108.
31 S. Datta, *Electronic Transport in Mesoscopic Systems*, Cambridge University Press, 1995.
32 S. Datta, *Nanotechnology*, 2004, **15**, S433.
33 S. Datta, *Quantum transport: atom to transistor*, Cambridge University Press, 2005.
34 R. J. C. Batista, M. S. C. Mazzoni, I. L. Garzón, M. R. Beltrán and H. Chacham, *Phys. Rev. Lett.*, 2006, **96**, 116802.
35 A. T. Lee, H. Park and S. Ismail-Beigi, *Phys. Rev. B: Condens. Matter Mater. Phys.*, 2021, **103**, 125105.
36 V.-H. Do and J.-M. Lee, *ACS Nano*, 2022, **16**, 17847–17890.
37 T. C. Siu, J. Y. Wong, M. O. Hight and T. A. Su, *Phys. Chem. Chem. Phys.*, 2021, **23**, 9643–9659.

